Journal of Asian Earth Sciences 111 (2015) 365–372

Contents lists available at ScienceDirect

Journal of Asian Earth Sciences

journal homepage: www.elsevier.com/locate/jseaes

Numerical earthquake models of the 2013 Nantou, Taiwan, earthquake series: Characteristics of source rupture processes, strong ground motions and their tectonic implication

Shiann-Jong Lee [a,*], Te-Yang Yeh [a], Hsin-Hua Huang [b,c], Cheng-Horng Lin [a]

[a] Institute of Earth Sciences, Academia Sinica, Taipei, Taiwan
[b] Department of Geology and Geophysics, University of Utah, Salt Lake City, UT, USA
[c] Seismological Laboratory, California Institute of Technology, Pasadena, CA, USA

ARTICLE INFO

Article history:
Received 4 March 2015
Received in revised form 11 June 2015
Accepted 30 June 2015
Available online 2 July 2015

Keywords:
Nantou earthquake series
Numerical earthquake model
Source rupture process
3-D wave propagation
Central Taiwan

ABSTRACT

On 27 March and 2 June 2013, two large earthquakes with magnitudes of M_L 6.2 and M_L 6.5, named the Nantou earthquake series, struck central Taiwan. These two events were located at depths of 15–20 km, which implied that the mid-crust of central Taiwan is an active seismogenic area even though the subsurface structures have not been well established. To determine the origins of the Nantou earthquake series, we investigated both the rupture processes and seismic wave propagations by employing inverse and forward numerical simulation techniques. Source inversion results indicated that one event ruptured from middle to shallow crust in the northwest direction, while the other ruptured towards the southwest. Simulations of 3-D wave propagation showed that the rupture characteristics of the two events result in distinct directivity effects with different amplified shaking patterns. From the results of numerical earthquake modeling, we deduced that the occurrence of the Nantou earthquake series may be related to stress release from the easternmost edge of a preexistent strong basement in central Taiwan.

1. Introduction

On the 27th of March 2013, a moderate-large earthquake (M_L 6.2) struck Nantou County in central Taiwan. About 2 months later, on the 2nd of June, a larger earthquake (M_L 6.5) again occurred at almost the same location. These two events were named the Nantou earthquake series in 2013 (also called the 0327 and 0602 events). Strong ground shakings were observed at Nantou County with a seismic intensity of 6 (250–400 gal), and many areas, including the densely-populated Taichung metropolitan, experienced a seismic intensity larger than 5 (80–250 gal). This earthquake series caused the collapse of three buildings, deaths of six people, and several injuries.

As shown in Fig. 1, the 2013 Nantou earthquake series occurred in a seismically active area, where several moderate to large earthquakes were recorded in the last century (also see Table 1). Between August 1916 and January 1917, three historical earthquakes (called the Nantou earthquake series in 1916–1917) occurred in this area with local magnitudes between M_L 6.2 and M_L 6.8. The location of a M_L 6.7 aftershock of the 1999 Chi-Chi earthquake in June 2000 (Kao and Chen, 2000; Chen et al., 2002; Chi and Dreger, 2004) was also in the vicinity of the 2013 Nantou earthquake series.

Both centroid moment tensors (CMT) of the two earthquakes provided by the Central Weather Bureau (CWB) show thrust faulting mechanisms with two north–south striking nodal planes, with one dipping toward the east with a shallower dipping angle, and the other dipping toward the west with a steeper fault plane (Fig. 1; also see Table 1). Several felt aftershocks had been recorded after the two events. The epicenters of the two aftershock sequences form two different alignment trends, one in the northwest–southeast direction and the other in the northeast–southwest direction. On the map (Fig. 1A), the patterns of aftershock distributions appear to be complementary in space even though the distance between the two mainshocks is less than 10 km. A cross section along c–c' is shown in Fig. 1B. These two events were located at depths of 15–20 km, which implied that the mid-crust of central Taiwan is an active seismogenic area even though there is no evidence show a subsurface structure directly related to any faults at surface.

A study of fault slip distributions of the Nantou earthquake series based on geodetic data proposed by Chuang et al. (2013) indicates that models with east-dipping fault planes can be most

* Corresponding author.
E-mail address: sjlee@earth.sinica.edu.tw (S.-J. Lee).

http://dx.doi.org/10.1016/j.jseaes.2015.06.031
1367-9120/

Table 1
Event list for moderate to large earthquakes in central Taiwan recorded in the last century.

	Date (yyyy/mm/dd)	Time[a] (hh:mi:ss)	Long. (°E)	Lat. (°N)	Depth (km)	Strike (°)	Dip (°)	Rake (°)	M_L
1	1916/08/28	15:27:00.0	121.00	24.00	45.0	–	–	–	6.8
1	1916/11/15	06:31:00.0	120.90	24.10	3.0	–	–	–	6.2
1	1917/01/05	00:55:00.0	121.00	24.00	–	–	–	–	6.2
1	1917/01/07	02:08:00.0	120.90	23.90	–	–	–	–	5.5
2	1999/09/21	01:47:15.9	120.82	23.85	8.0	3	30	66	7.3
2	2000/06/11	02:23:29.5	121.11	23.90	16.2	355	17	63	6.7
3	2013/03/27	10:03:19.6	121.05	23.90	19.4	355	25	75	6.2
3	2013/06/02	13:43:03.2	120.97	23.86	14.5	2	29	83	6.5

[1]Nantou earthquake series in 1916–1917 (taken from Central Weather Bureau historical earthquake catalog).
[2]1999 Chi-Chi earthquake mainshock and its biggest aftershock.
[3]Nantou earthquake series in 2013.
[a] Taiwan standard time (UT + 8).

likely compatible with the observations. The slips were concentrated at depths between 9 and 16 km, with primarily reverse, updip slip. Their results provide static slip patterns of the two events. In this study, we investigated the numerical earthquake models of the Nantou earthquake series, including their detailed rupture time history and the generation of strong ground motions. Joint source inversions by using teleseismic, near-field strong motion, and GPS coseismic data were first carried out. Unlike geodetic inversion, which can only provide the total slip pattern, the three data sets used in this joint inversion can constrain both the details of the rupture process (by waveform data) and the total slip pattern (by geodetic data). Then, using the source inversion results as the input rupture models, 3-D wave propagation simulations were performed for the Taiwan region. Using precise numerical earthquake models, the nucleation of this earthquake series, propagation of strong ground shaking, and mechanism of the seismogenic area in central Taiwan are discussed. The results of this study could also be applied to the worldwide areas where have similar case of basement boundary earthquakes as well as hazard assessment, such as the 1909 Lambasc (Provence, France) earthquake (Chardon and Bellier, 2003), the Kitayuri thrust system in northeast Honshu, Japan (Awata and Kakimi, 1985), and southern California (Shaw et al., 2015).

2. Source rupture models

2.1. Data

To understand the mechanisms of the Nantou earthquake serious, we investigated the rupture processes of these two events based on joint source inversion. Three data sets were used in the inversion, including teleseismic body wave, near field GPS coseismic displacement and ground motion data. The teleseismic data have good data quality and azimuthal coverage to the earthquake which provide a first-order determination of fault rupture behavior. The near-field GPS coseismic deformation data provide a good constraint on the total spatial slip pattern. In addition, the two events are well recorded by dense regional seismic networks, which can provide further constraints on the temporal rupture processes.

Eighteen and sixteen teleseismic stations were used for the 0327 and 0602 event, respectively. The stations provided good azimuthal coverage and were located between 30° and 90° to avoid the complex earth structure (distributions of the stations can be found in supplementary Figs. S1.1 and S2.1). These data were digital recordings obtained from IRIS (the Incorporated Research Institutions for Seismology). Signals were deconvolved from the instrument response, re-sampled to 10 points per second and a band-pass filter (0.01–0.5 Hz) was applied. We used a time window of 25–30 s after the *P* arrival time with an addition of 10 s before the *P* arrival. The GPS coseismic displacements used in this study were compiled by TEC GPS Lab (http://gps.earth.sinica.edu.tw). There were 316 sites of three-component GPS coseismic displacements. We selected displacements with standard deviation less than 10 mm in all three components to be used in the inversion. Near field seismic records were from Broadband Array in Taiwan for Seismology (BATS) and CWB real-time strong motion data (RTD). These two data sets provided a good azimuthal coverage around the source area. We considered velocity seismic records in the inversion, all the strong motion data were integrated from acceleration to velocity, and then band-pass filtered between 0.05 Hz and 0.2 Hz. In total, 32 records were selected for the 0327 event and 40 records were considered for the 0602 event. We used a waveform time-window of 35–50 s that starts from the event original time with a sampling rate of 0.1 s.

2.2. Method

The finite fault source inversion problem is usually formulated in a linear form, $\mathbf{Ax} = \mathbf{b}$ where $\mathbf{A}$ is the matrix of Green's functions, $\mathbf{b}$ is the observed data vector and $\mathbf{x}$ is the solution vector of slip characteristics on each subfault, including amplitude, direction and rupture time (Hartzell and Heaton, 1983). We applied the multiple-time windows technique in the inversion procedure that provides a more detailed slip spatial and temporal resolution. The program performance was improved by using a parallel Non-Negative Least-Squares (NNLS) inversion technique (Lee et al., 2006). A misfit function, defined as $(\mathbf{Ax}-\mathbf{b})^2/\mathbf{b}^2$, was used to evaluate the quality of a solution.

In matrix $\mathbf{A}$, the teleseismic Green's functions were calculated by using the approach developed by Kikuchi and Kanamori (1982), where the near source structure was given by using a 1-D Taiwan average crust model (Chen and Shin, 1998) while the receiver side structure used a global 1-D IASPEI91 model (Kennett and Engdahl, 1991). The teleseismic synthetic waveforms were filtered between 0.01 and 0.5 Hz. For the geodetic Green's functions, we used the analytic expressions of Okada (1992) to calculate the horizontal and vertical static displacements where surface deformation results from a uniform slip over each subfault. The 3-D synthetic Green's functions for near field ground motion station was generated by the spectral-element method (SEM, Komatitsch and Tromp, 1999; Komatitsch et al., 2004), with a tomography velocity model taken from Huang et al. (2014). The seismic synthetic waveforms were filtered between 0.05 and 0.2 Hz in the same frequency range as for observed data.

In the inversion, we used 28 time windows of 0.2 s length, each window overlapping 0.1 s, leading to each subfault the possibility to slip within 2.9 s after the rupture starts. A maximum rupture velocity, $Vr = 3.0$ km/s, was assumed to approximate the full

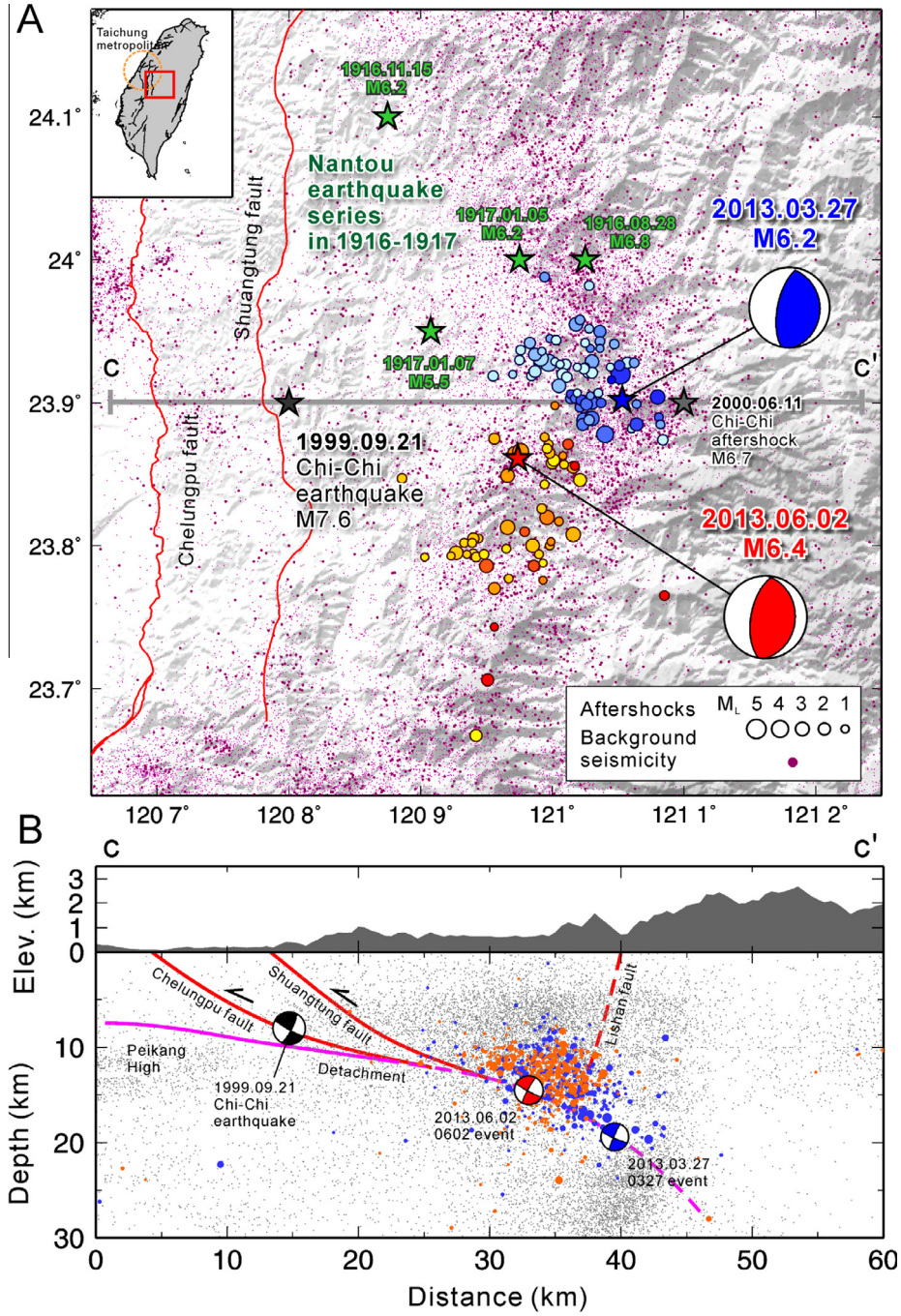

Fig. 1. (A) The location map of the Nantou earthquake series. The blue star indicates the epicenter of the 0327 event and the red star represents the 0602 event. Aftershocks of the 0327 and 0602 events are shown by the cold and hot colored circles, respectively. The epicenters of the 1916–1917 Nantou earthquake series are shown by the green stars. The 1999 Chi-Chi earthquake mainshock and its largest aftershock are shown with black and gray stars, respectively. The purple dots denote background seismicity recorded from 1901 to 2013 reported by the CWB. Detailed source parameters of major earthquakes in central Taiwan recorded in the last century are provided in Table 1. (B) Vertical cross section along c–c' profile. The blue beach ball shows the 0327 event, the red beach ball denotes the 0602 event, and the black beach ball is the 1999 Chi-Chi earthquake. Aftershocks of the 0327 and 0602 events are shown by the blue and orange colored circles, respectively. (For interpretation of the references to color in this figure legend, the reader is referred to the web version of this article.)

time–space inversion (Lee et al., 2006). Two north–south striking, eastern dipping fault planes characterized by thrust movement (strike 355°, dip 25° and rake 75° for 0327 event; strike 2°, dip 29° and rake 83° for 0602 event) taken from the CWB earthquake report were considered. The fault planes were divided into 3×3 km^2 subfaults for finite-fault approach. The slip on each subfault was divided into rake ±45° in the inversion. Thus, the variation of rake angle on each subfault can be determined by the combination of these two slip components.

2.3. Inversion results

Slip distributions determined from the joint source inversion for the two events are shown in Figs. 2 and 3. Detailed descriptions of data fittings are provided in the supplementary material. The rupture of the 0327 event mainly occurred in an area that had an oblong shape in which one asperity was identified (Fig. 2). The initial rupture developed in a deeper part at about a depth of 20 km close to the hypocenter, and the asperity was located at about a

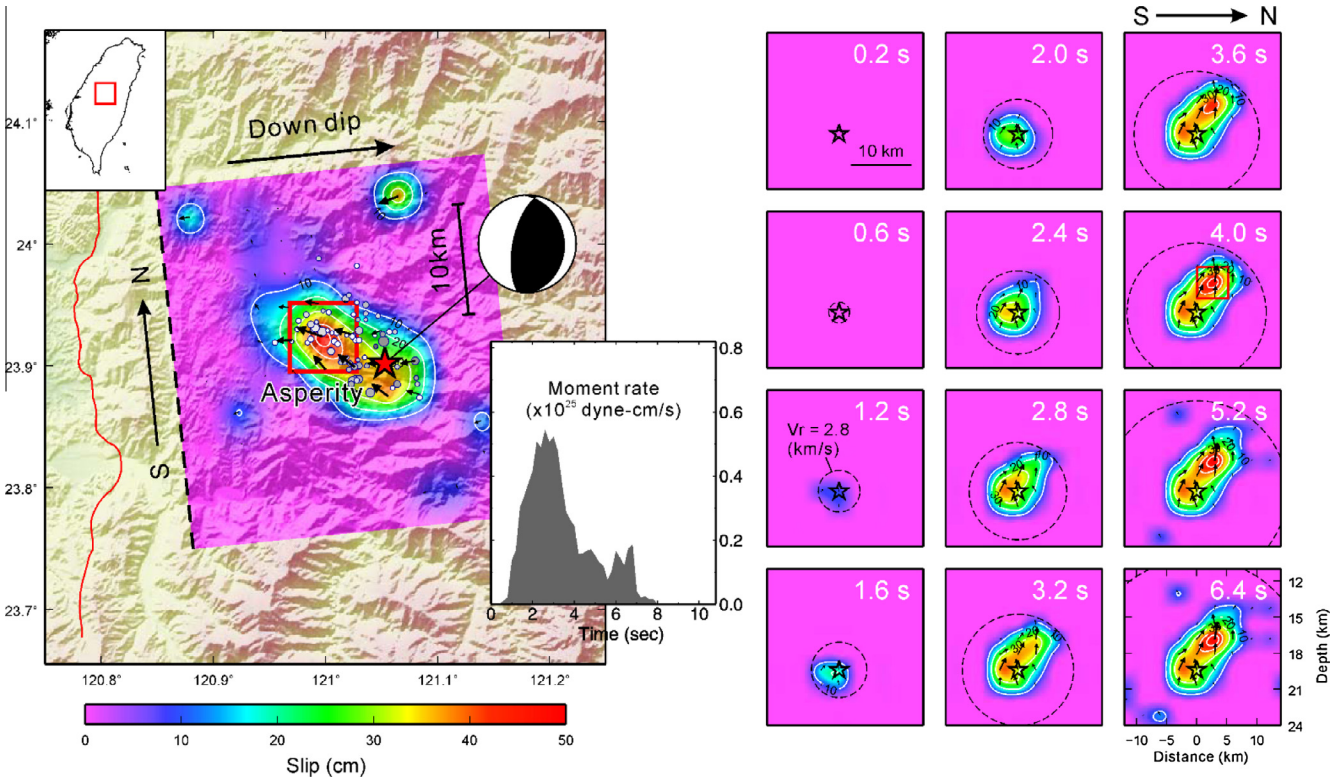

Fig. 2. Source inversion results of the 0327 event. The panels from the left to the right illustrate the map view of slip distribution (left), moment rate function (middle), and rupture snapshots (right). The dotted open circles in the rupture snapshots indicate reference rupture fronts (Vr = 2.8 km/s).

depth of 15–18 km. Slips in the rupture area were predominately thrust movement. Average slip on the fault plane determined from the joint inversion was about 25.9 cm and the maximum slip was 48.7 cm as observed on the asperity. From the map view of the

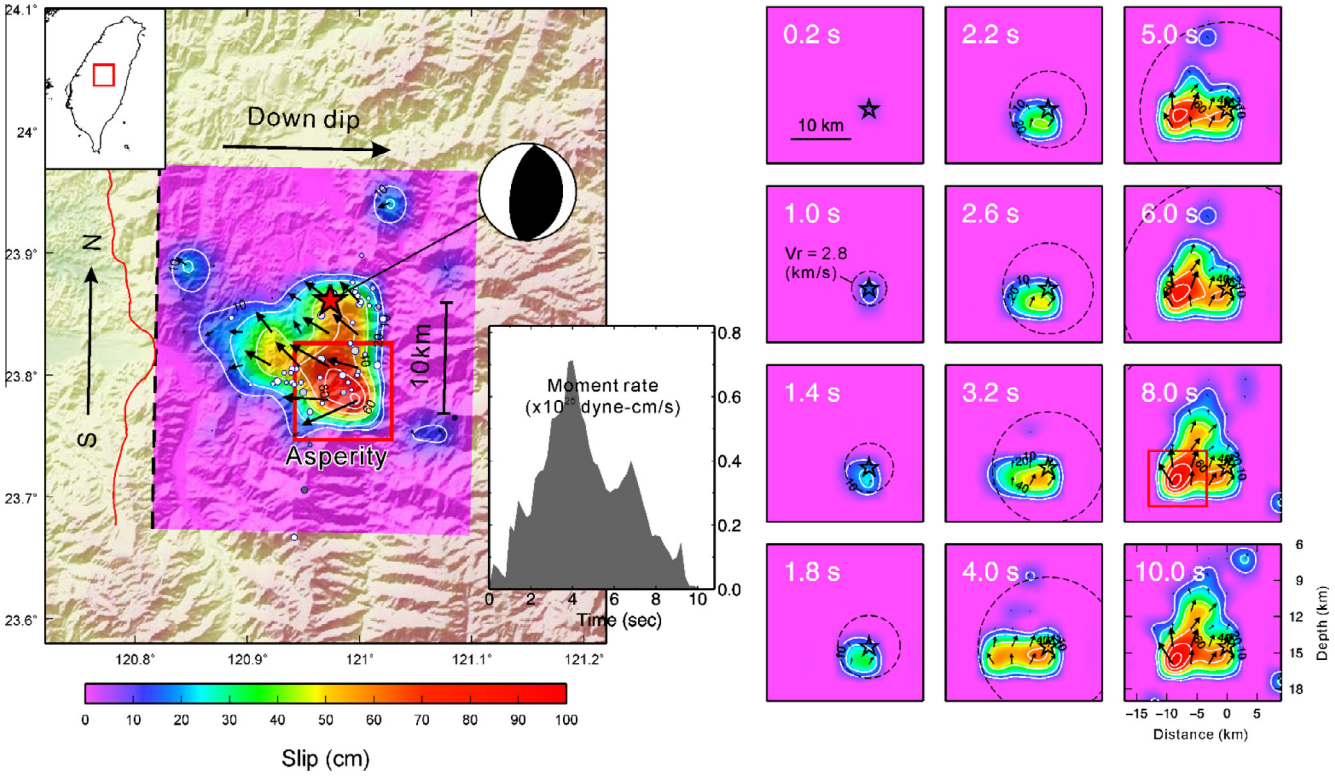

Fig. 3. Source inversion results of the 0602 event. The panels from the left to the right are the map view of slip distribution (left), moment rate function (middle), and rupture snapshots (right). The dotted open circles indicate reference rupture fronts with a constant rupture velocity Vr = 2.8 km/s.

fault projected to the ground surface, both slip and aftershock distributions show a northwest–southeast linear trend. The rupture snapshot shows that the rupture initiated at the hypocenter in the middle crust of about 20 km, then propagated to the shallow crust (~14 km) in the northwest direction. The source time function of the entire rupture was approximately a triangular shape with a duration of about 6 s. The total seismic moment was 0.169×10^{19} Nm, which is equivalent to an earthquake of M_w 6.08.

The slip distribution of the 0602 event shows a more complex pattern and the rupture region covers a larger area compared to those of the 0327 event. Most of the slip occurred in the left portion of the fault plane (in the southwestern portion of the fault plane from map view, see Fig. 3). An asperity with a maximum slip of about 106.7 cm was observed south of the hypocenter. The rupture initiated from the hypocenter, then ruptured to the south and formed a large asperity after about 5 s. The rupture then extended to the shallower fault plane until the entire process was completed. The source time function of the 0602 event was also close to a triangular shape with a longer duration of about 10 s. The total seismic moment was 0.293×10^{19} Nm, which is equivalent to an earthquake of M_w 6.25. Assuming a circular fault model, the estimated stress drops $\Delta\sigma$ of the 0327 and 0602 events were 2.16 MPa and 2.95 MPa, respectively.

3. 3-D wave propagation models

To further understand the details of ground motion characteristics of these two events, we performed forward simulations with the source models derived from the previous inversion results. The simulations were based on the spectral-element method (SEM). The SEM mesh model employed incorporates surface topography, basin geometry, and 3-D wave-speed heterogeneity (Lee et al., 2014). The surface topography based on 40 m digital elevation model data is implemented at the top of the SEM mesh model (Lee et al., 2009). The 3-D basin geometry and the related wave-speed model are derived from Wang et al. (2004). We embed the basin model in a regional tomographic model derived by Huang et al. (2014). Considering the resolutions of the numerical mesh and the velocity models used, the simulation is capable of

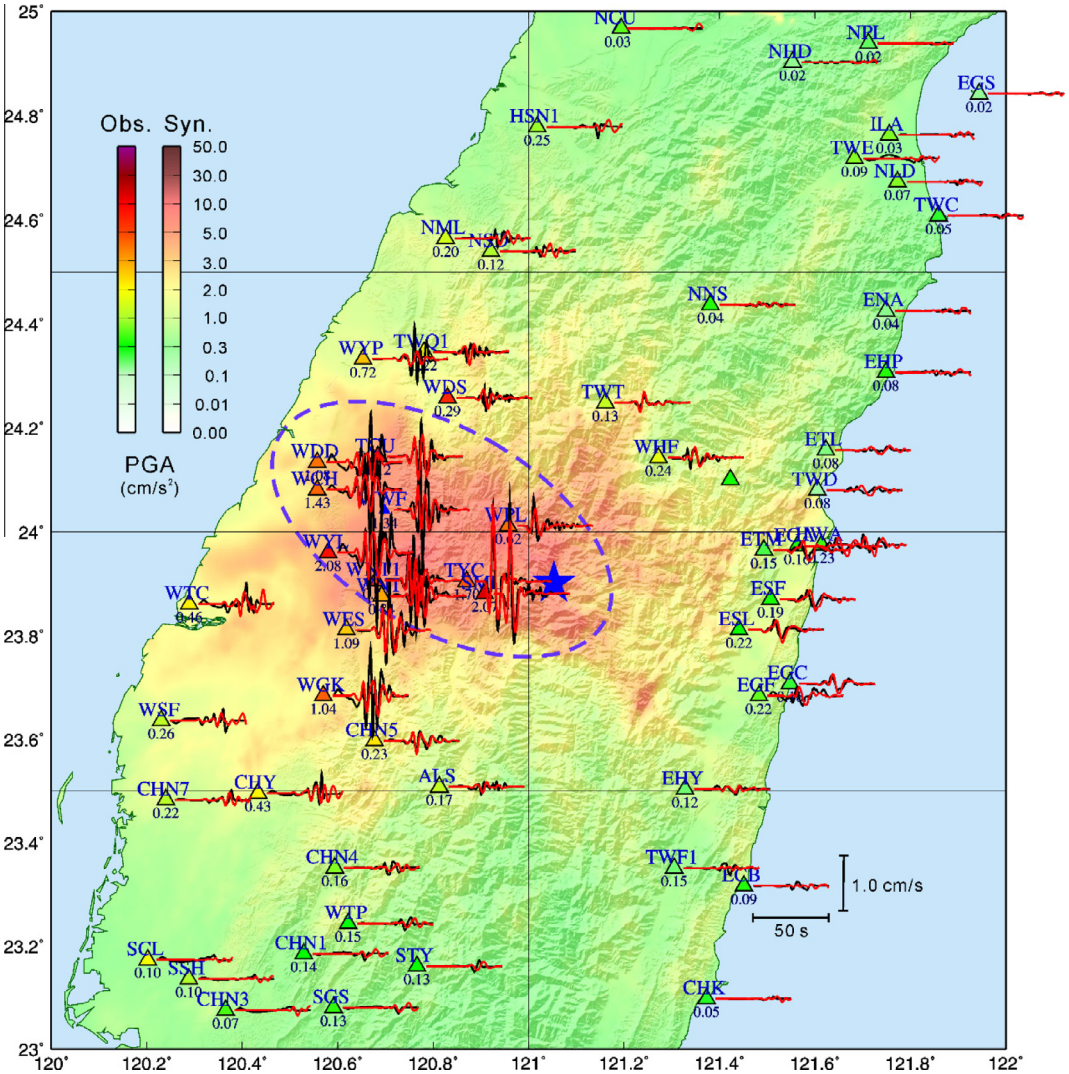

Fig. 4. Comparison between the observed and synthetic velocity waveforms for the east–west component in the 0327 even. The black lines denote the observations, while the red lines represent the synthetics. All the waveforms are band-pass filtered between 0.05 and 0.2 Hz. The number in front of each waveform indicates the peak value of observation. The background shows the ShakeMap of the simulation result, which is obtained from the norm of all three components of the acceleration wavefield (at about 1 Hz). The colored triangles show the norm of peak acceleration of observed data, low-pass filtered to 1 Hz for comparison. The open dotted circle indicates the strong shaking areas of the 0327 event.

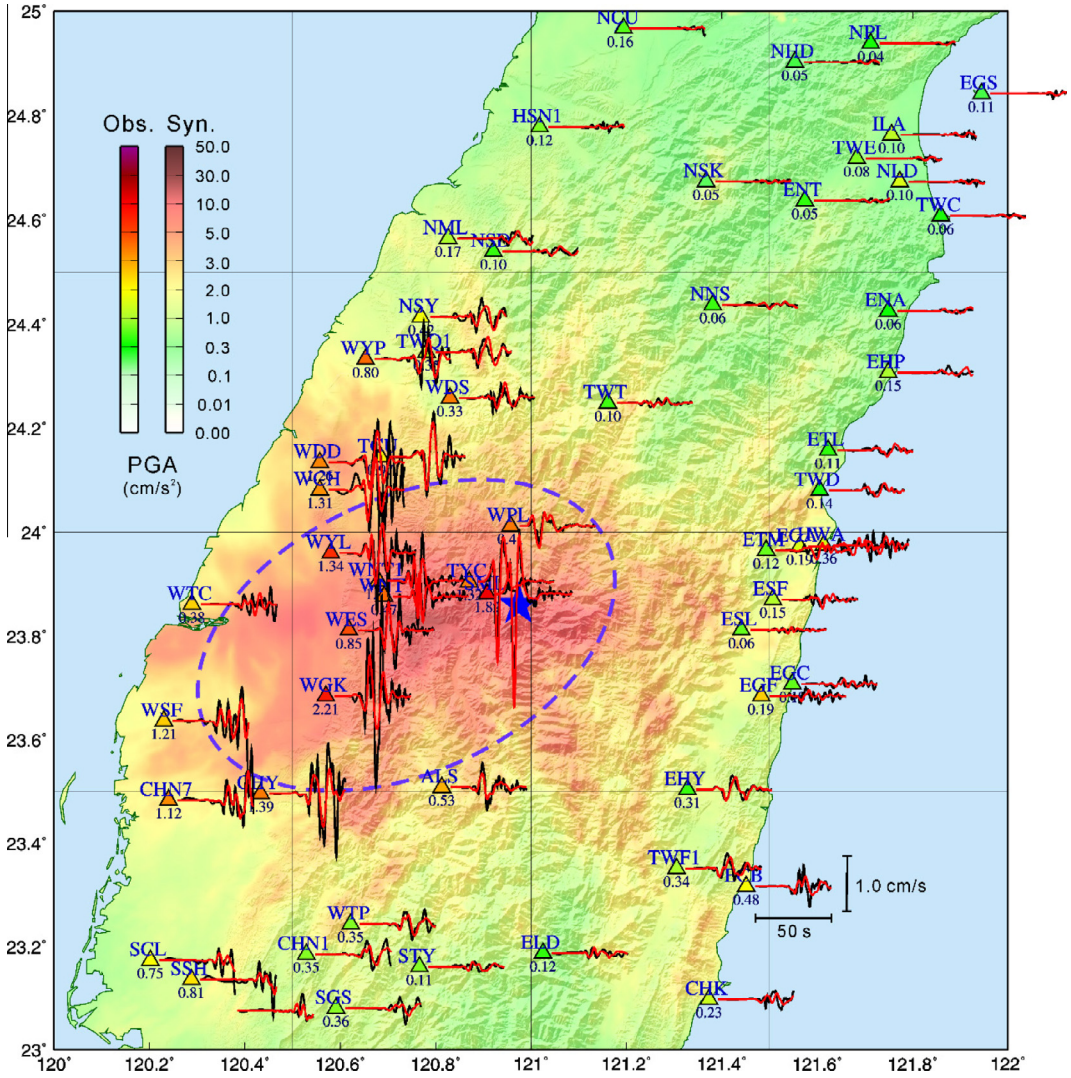

Fig. 5. Comparison between the observed and synthetic velocity waveforms for the north–south component in the 0602 event. The black lines denote the observations, and the red lines represent the synthetics. All the waveforms are band-pass filtered between 0.05 and 0.2 Hz. The number in front of each waveform indicates the peak value of observation. The background shows the ShakeMap of the simulation result obtained from the norm of all three components of the acceleration wavefield at about 1 Hz. The colored triangles show the norm of peak acceleration of observed data (low-pass filtered to 1 Hz). The open dotted circle points out the strong shaking areas of the 0602 event. (For interpretation of the references to color in this figure legend, the reader is referred to the web version of this article.)

representing 3-D wavefield and synthetic waveforms accurate up to 1 Hz.

The ShakeMaps for the norm of peak acceleration of the two events are displayed in Figs. 4 and 5. The ground shaking in the western side of the source area was much stronger than in the eastern side in both events. This could partly be attributed to the radiation pattern corresponding to a thrust movement on an eastern dipping fault plane. In addition, the ruptures of the two earthquakes have remarkable rupture directions – they both ruptured to the west from the middle to the shallow crust in the derived source models. Consequently, strong directivity effects were observed which lead to elongated patterns in their shaking maps. For the 0327 event, the region with strong shaking covered the source area and extended to its northwestern side (Fig. 4). Meanwhile, for the 0602 event, strong shakings could be observed not only in the source area but also extended to a large area southwest of the epicenter (Fig. 5). These simulation results are consistent with the norm of the observed peak ground acceleration (PGA) values (low-pass filtered by 1 Hz) recorded by the CWB RTD as shown by the different colored triangles in Figs. 4 and 5. In addition, the characteristics of synthetic PGA patterns of the two events are also compatible with the PGA distributions derived from the free-field strong-motion records (Wen et al., 2014) and the Palert system (Hsieh et al., 2014).

Comparisons between the RTD velocity data and forward synthetic waveforms calculated from the inverted source model are provided in Figs. 4 and 5. Results show that both the timings and waveform characteristics of synthetics were comparable to the observations for the period between 5 and 20 s. The waveforms observed in western Taiwan (e.g., stations TCU, WES, WGK) are usually characterized by stronger amplitudes and more complex phases compared to those in eastern Taiwan (e.g., stations ETL, ESL, EHY). They were mainly due to the directivity effect with the westward updip rupture direction. The shallow low-velocity sedimentary deposit in western Taiwan may also have played an important role in amplifying the ground shaking further. On the other hand, the waveforms in the north and south of Taiwan showed smaller amplitudes in both events. These waveform characteristics were well modeled by the forward synthetics. The waveform misfits between observations and forward synthetics

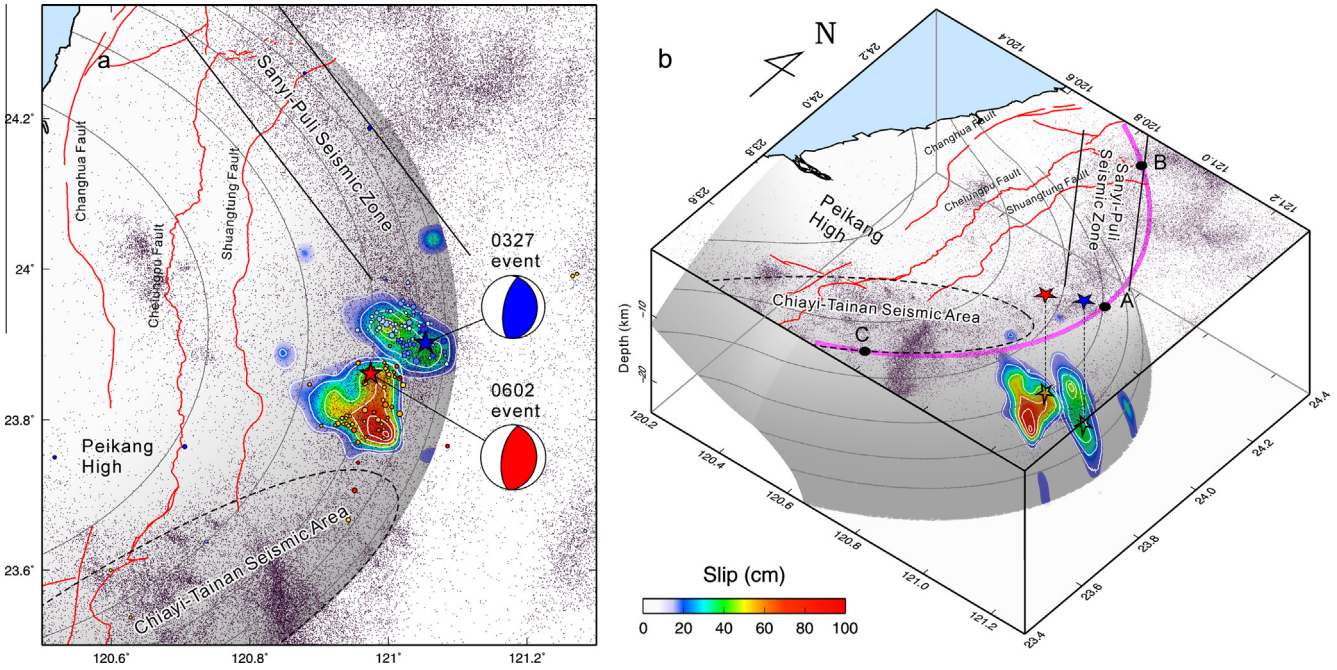

Fig. 6. (a) The map view of the inverted 0327 and 0602 slip distributions projected to the ground surface with active faults (red lines), background seismicity (purple dots), and strong basement (convex contours). (b) A 3-D schematic plot of the relationship between the strong basement, low seismicity block, and the slip distributions of the 2013 Nantou earthquake series. Pink convex contour indicates the boundary of the strong basement projected to the ground surface. (For interpretation of the references to color in this figure legend, the reader is referred to the web version of this article.)

for 0327 and 0602 events are 0.72 and 0.67, respectively. Such comparable fits in waveforms indicate that both the details of the source rupture models and the 3-D velocity model are precise enough to reproduce the main characteristics of strong ground motions of the Nantou earthquake series for simulations accurate up to 0.2 Hz.

4. Discussion and conclusions

The combined slip distribution of the Nantou earthquake series is shown as a map view in Fig. 6. Although the epicenters of the two events were close (<10 km), their rupture areas and aftershocks were not overlapping each other. The rupture of the 0327 event generally propagated toward a northwestern direction while that of the 0602 event ruptured toward a southwestern direction. It is worthwhile to note that the aftershock distributions also followed these patterns. The slip area of the 0327 event, which was about 153 km^2 with a maximum slip of about 48.7 cm, was smaller than that of the 0602 event, which had a larger size of 180 km^2 and a maximum slip of about 106.7 cm. This is also represented in their inverted moment magnitude (a moment magnitude of M_w 6.08 for the 0327 event and a bigger magnitude of M_w 6.25 for the 0602 event).

By superimposing the slip distributions, aftershocks, and background seismicity together, an interesting pattern related to the two events can be observed (Fig. 6). From the background seismicity, a convex curve, low seismicity block exists in central Taiwan that is bounded by the Sanyi-Puli Seismic Zone in the northeast part and Chiayi-Tainan Seismic Area in the southeast. In the map view (Fig. 6a), these two seismogenic zones are located on the edge of a strong basement, named Peikang High (Tang, 1977). This basement high was previously found beneath the Coastal Plain, and the deepest depth is less than 10 km. However, the detailed geometry has not been well established, especially at the eastern side of the Chelungpu fault beneath the Western Foothill. Spatially, the 0327 event was located at the southeast tip of the Sanyi-Puli Seismic Zone, and the 0602 event occurred at the northeasternmost part of the Chiayi-Tainan Seismic Area. A 3-D schematic plot of the slip distributions belonging to the two events projected onto the strong basement is shown in Fig. 6b. As can be seen, the hypocenter of the 0327 event is located at a deeper depth of about 20 km, and that of the 0602 event is at a shallower depth of about 15 km. According to the evidence discovered, we can conclude that the ruptures of these two events occurred at an eastern-dipping ramp, which can be considered as the eastern extension boundary of the strong basement.

Lin (2001) proposed a heel-shaped model to explain the seismogenic process of the 1999 Chi-Chi earthquake (M_w 7.6). It is defined by the previously discussed convex curve, low seismicity block, and the surface ruptures along the Chelungpu fault. Stress focusing due to partitioning along the convex curve most likely took place at the hypocenter of the Chi-Chi earthquake. On the contrary, the occurrence of the 2013 Nantou earthquake series was likely due to the stress accumulation at the easternmost tip of the strong basement where the convergent vector was almost perpendicular to the eastern dipping edge.

Based on these inferences and the results of this study, a critical issue with seismic hazard assessment in central Taiwan could be deduced. According to the geodetic observations as previously mentioned, the strain energy can accumulate at the eastern tip of the strong basement (Location A in Fig. 6b) along the principle axis direction. A large amount of strain energy being stored in the middle crust over decades can cause moderate to large earthquakes upon release. The occurrence of the 1916–1917 Nantou earthquake series (M_L 5.5–6.8) and the 2013 Nantou earthquake series (M_L 6.2 and M_L 6.5) could be attributed to this reason. On the other hand, the strain can also be partitioned into two flanks along the convex boundary (Locations B and C in Fig. 6b). Due to the fact that these boundaries in the middle depth of the crust are not perpendicular to the orientation of the local strain field, smaller events could take place frequently in the northern portion (Sanyi-Puli Seismic Zone) and the southern portion (Chiayi-Tainan Seismic Area).

As known from the source inversion results in this study, the events which occurred at the easternmost tip of the strong basement, could mainly have ruptured in the east-to-west direction, with thrust and updip movements on eastern dipping fault planes. This rupture behavior can cause the striking directivity effect, which amplifies the shaking in the western side from the source area. It leads to large ground motions which will propagate toward the Taichung metropolitan area in western Taiwan as was observed in the 2013 Nantou earthquake series. Thus, this type of moderate-large, mid-crust thrust event in central Taiwan should be considered seriously in future earthquake scenario analyses for the purpose of seismic hazard assessment.

Acknowledgements

The Real-time strong motion data (RTD) for this paper are available at Taiwan Rapid Earthquake Information Release System implemented by the Central Weather Bureau. The teleseismic data used was obtained from Incorporated Research Institutions for Seismology (IRIS). The GPS coseismic displacements are available at TEC GPS Lab (http://gps.earth.sinica.edu.tw). Our research was supported by Academia Sinica funded through the Taiwan Numerical Earthquake Model (TNEM) project, Grant Number 102-Investigator Award-02. This research was also supported by the Taiwan Earthquake Research Center funded through the Ministry of Science and Technology by Grant Number MOST 103-2628-M-001-004-MY3. The TEC contribution number for this article is 00115.

Appendix A. Supplementary material

Supplementary data associated with this article can be found, in the online version, at http://dx.doi.org/10.1016/j.jseaes.2015.06.031.

References

Awata, Y., Kakimi, T., 1985. Quaternary tectonics and damaging earthquakes in northeast Honshu, Japan. Earthquake Prediction Res. 3, 231–251.

Chardon, D., Bellier, O., 2003. Geological boundary conditions of the 1909 Lambesc (Provence, France) earthquake: structure and evolution of the Trévaresse ridge anticline. Bulletin de la Société Géologique de France 174, 497–510.

Chen, K.C., Huang, B.S., Wang, J.H., Yen, H.Y., 2002. Conjugate thrust faulting associated with the 1999 Chi-Chi, Taiwan, earthquake sequence. Geophys. Res. Lett. 29, 1277. http://dx.doi.org/10.1029/2001GL014250.

Chen, Y.L., Shin, T.C., 1998. Study of the earthquake location of 3-D velocity structure in Taiwan area. Meteoritical Bull. 42, 135–169.

Chi, W.C., Dreger, D., 2004. Crustal deformation in Taiwan: results from finite source inversions of six M_w > 5.8 aftershocks. J. Geophys. Res. 109. http://dx.doi.org/10.1029/2003JB002606.

Chuang, R.Y., Johnson, K.M., Wu, Y.M., Ching, K.E., Kuo, L.C., 2013. A midcrustal ramp-fault structure beneath the Taiwan tectonic wedge illuminated by the 2013 Nantou earthquake series. Geophys. Res. Lett. 40, 5080–5084. http://dx.doi.org/10.1002/grl.51005.

Hartzell, S.H., Heaton, T.H., 1983. Inversion of strong ground motion and teleseismic waveform data for the fault rupture history of the 1979 Imperial Valley, California earthquake. Bull. Seismol. Soc. Am. 73, 1553–1583.

Hsieh, C.Y., Wu, Y.M., Chin, T.L., Kuo, K.H., Chen, D.Y., Wang, K.S., Chan, Y.T., Chang, W.Y., Li, W.S., Ker, S.H., 2014. Low cost seismic network practical applications for producing quick shaking maps in Taiwan. Terrestrial, Atmos. Oceanic Sci. 25 (5), 617–624.

Huang, H.H., Wu, Y.M., Song, X., Chang, C.H., Lee, S.J., Chang, T.M., Hsieh, H.H., 2014. Joint Vp and Vs tomography of Taiwan: implications for subduction-collision orogeny. Earth Planet. Sci. Lett. 392, 177–191.

Kao, H., Chen, W.P., 2000. The Chi-Chi earthquake sequence of September 20, 1999 in Taiwan: seismotectonics of an active, out-of sequence thrust. Science 288, 2346–2349.

Kennett, B.L.N., Engdahl, E.R., 1991. Traveltimes for global earthquake location and phase identification. Geophys. J. Int. 122, 429–465.

Kikuchi, M., Kanamori, H., 1982. Inversion of complex body waves. Bull. Seismol. Soc. Am. 72, 491–506.

Komatitsch, D., Liu, Q., Tromp, J., Süss, P., Stidham, C., Shaw, J.H., 2004. Simulations of ground motion in the Los Angeles basin based upon the spectral-element method. Bull. Seismol. Soc. Am. 94, 187–206.

Komatitsch, D., Tromp, J., 1999. Introduction to the spectral-element method for 3-D seismic wave propagation. Geophys. J. Int. 139, 806–822.

Lee, S.J., Komatitsch, D., Huang, B.S., Tromp, J., 2009. Effects of topography on seismic wave propagation: an example from northern Taiwan. Bull. Seismol. Soc. Am. 99, 314–325. http://dx.doi.org/10.1785/0120080020.

Lee, S.J., Liu, Q., Tromp, J., Komatitsch, D., Liang, W.T., Huang, B.S., 2014. Toward real-time regional earthquake simulation II: real-time online earthquake simulation (ROS) of Taiwan earthquakes. J. Asian Earth Sci. 87, 56–68.

Lee, S.J., Ma, K.F., Chen, H.W., 2006. Three-dimensional dense strong motion waveform inversion for the rupture process of the 1999 Chi-Chi, Taiwan, earthquake. J. Geophys. Res. 111, B11308. http://dx.doi.org/10.1029/2005JB004097.i.

Lin, C.H., 2001. The 1999 Taiwan earthquake: a proposed stress-focusing, heel-shaped model. Bull. Seismol. Soc. Am. 91, 1053–1061.

Okada, Y., 1992. Internal deformation due to shear and tensile faults in a half-space. Bull. Seismol. Soc. Am. 82, 1018–1040.

Shaw, J.H., Plesch, A., Tape, C., Suess, M.P., Jordan, T.H., Ely, G., Hauksson, E., Tromp, J., Tanimoto, T., Graves, R., Olsen, K., Nicholson, C., Maechling, P.J., Rivero, C., Lovely, P., Brankman, C.M., Munster, J., 2015. Unified structural representation of the southern California crust and upper mantle. Earth Planet. Sci. Lett. 415, 1–15. http://dx.doi.org/10.1016/j.epsl.2015.01.016.

Tang, C.H., 1977. Late miocene erosional unconformity on the subsurface Peikang High beneath the Chiayi-Yunlin, Coastal Plain, Taiwan. Mem. Geol. Soc. China 2, 155–167.

Wang, C.Y., Lee, Y.H., Ger, M.L., Chen, Y.L., 2004. Investigating subsurface structures and P- and S-wave velocities in the Taipei basin. Bull. Seismol. Soc. Am. 15, 222–250.

Wen, Y.Y., Miyake, H., Yen, Y.T., Irikura, K., Ching, K.E., 2014. Rupture directivity effect and stress heterogeneity of the 2013 Nantou blind-thrust earthquakes, Taiwan. Bull. Seismol. Soc. Am. 104, 2933–2942. http://dx.doi.org/10.1785/0120140109.